Self-organized stress patterns drive state transitions in actin cortices

Tzer Han Tan, Maya Malik-Garbi, Enas Abu-Shah, Junang Li, Abhinav Sharma, Fred C. MacKintosh, Kinneret Keren, Christoph F. Schmidt, Nikta Fakhri

BIOPHYSICS

Self-organized stress patterns drive state transitions in actin cortices

Tzer Han Tan[1]*, Maya Malik-Garbi[2]*, Enas Abu-Shah[2,3]*, Junang Li[1], Abhinav Sharma[4,5]†,
Fred C. MacKintosh[4,6,7], Kinneret Keren[2,3,8]‡, Christoph F. Schmidt[5,9,10]‡, Nikta Fakhri[1]‡

Biological functions rely on ordered structures and intricately controlled collective dynamics. This order in living systems is typically established and sustained by continuous dissipation of energy. The emergence of collective patterns of motion is unique to nonequilibrium systems and is a manifestation of dynamic steady states. Mechanical resilience of animal cells is largely controlled by the actomyosin cortex. The cortex provides stability but is, at the same time, highly adaptable due to rapid turnover of its components. Dynamic functions involve regulated transitions between different steady states of the cortex. We find that model actomyosin cortices, constructed to maintain turnover, self-organize into distinct nonequilibrium steady states when we vary cross-link density. The feedback between actin network structure and organization of stress-generating myosin motors defines the symmetries of the dynamic steady states. A marginally cross-linked state displays divergence-free long-range flow patterns. Higher cross-link density causes structural symmetry breaking, resulting in a stationary converging flow pattern. We track the flow patterns in the model actomyosin cortices using fluorescent single-walled carbon nanotubes as novel probes. The self-organization of stress patterns we have observed in a model system can have direct implications for biological functions.

INTRODUCTION

The cell cortex is a quasi–two-dimensional (2D) dissipative structure of dynamically cross-linked actin filaments that continuously polymerize and depolymerize (1, 2). This network is anchored to the cell membrane and is internally activated by myosin motor proteins and affected by external forces exerted by the cellular environment (1). The cortex provides mechanical integrity and rigidity to cells over extended time scales, while its components turn over within minutes (3–6). In addition, the cortex undergoes marked reorganizations during cellular processes such as division, generation of polarity, and motility (7–9). These processes often entail transitions from homogeneous to inhomogeneous states via network contraction (10, 11) and typically display marked fluctuations (12–16). An intriguing question is how the cortex achieves the feat of switching between stability and large-scale reorganization.

Cortex structure and dynamics are controlled by a subtle interplay between actin turnover and network connectivity, as well as strains and stresses generated by nonmuscle myosin motors, all regulated by complex biochemical pathways (17–20). Characteristic time scales of biochemical kinetics are on the order of seconds (17, 21, 22). A quantitative understanding of cortical dynamics requires experimental model systems in which one can decouple biochemical signaling from network dynamics. A bottom-up reconstitution of a realistic model cortex from minimal components has not been achieved. Reconstitution of myosin-driven actin solutions has displayed interesting dynamics (11, 23–25) but remains far from real cortex, primarily because of the lack of actin turnover.

Experimental access to the active mechanics of cellular and model cortices has been severely limited. Techniques such as atomic force microscopy indentation (26) or pipette aspiration (27) only provide global, coarse-grained measurements, not capturing spatial inhomogeneity, anisotropy, and time dependence (17). Microrheology (28) could, in principle, provide local information, but its use in the cortex has been limited by the lack of suitable probes; micrometer-sized colloidal beads are too large to penetrate the thin cortex without perturbing it, while nanometer-sized particles, such as quantum dots, are too small to remain in the network for long enough to probe it. Here, we use high–aspect ratio single-walled carbon nanotubes (SWNTs) as "stealth" probes. Using this novel approach, we discover that a subtle interplay between mechanical percolation of the network and propagation of myosin-generated stresses leads to structurally and dynamically distinct steady states in model actomyosin cortices.

[1]Department of Physics, Massachusetts Institute of Technology, Cambridge, MA 02139, USA. [2]Department of Physics, Technion—Israel Institute of Technology, Haifa, Israel. [3]Russell Berrie Nanotechnology Institute, Technion—Israel Institute of Technology, Haifa, Israel. [4]Department of Physics and Astronomy, Vrije Universiteit, Amsterdam, Netherlands. [5]Third Institute of Physics—Biophysics, University of Göttingen, Göttingen, Germany. [6]Department of Chemical and Biomolecular Engineering, Rice University, Houston, TX 77005, USA. [7]Center for Theoretical Biophysics, Rice University, Houston, TX 77005, USA. [8]Network Biology Research Laboratories, Technion—Israel Institute of Technology, Haifa, Israel. [9]German Center for Cardiovascular Research (DZHK), Göttingen, Germany. [10]Department of Physics, Duke University, Durham, NC 27708, USA.
*These authors contributed equally to this work.
†Present address: Leibniz Institute for Polymer Research, Hohe Strasse 6, 01069 Dresden, Germany.
‡Corresponding author. Email: kinneret@physics.technion.ac.il (K.K.); christoph.schmidt@phys.uni-goettingen.de (C.F.S.); fakhri@mit.edu (N.F.)
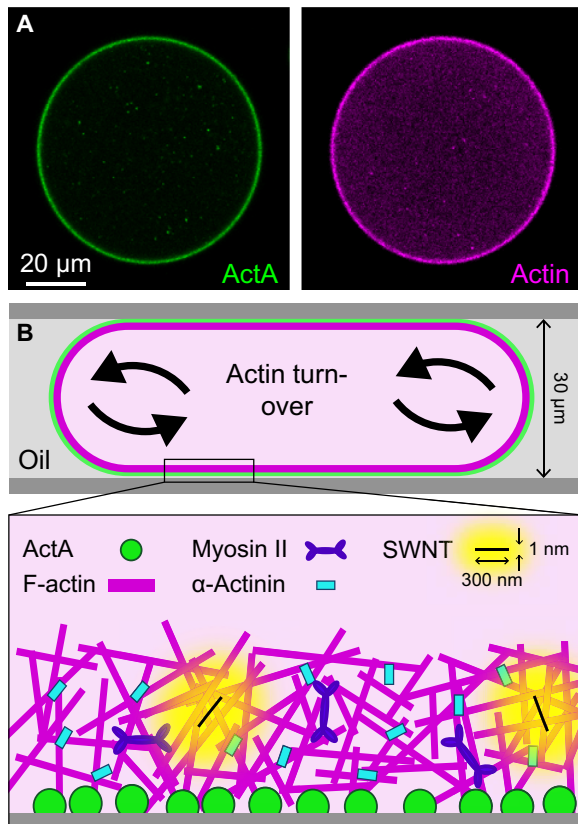
RESULTS

We formed dynamic cortices in vitro by encapsulating *Xenopus* egg extract in water-in-oil emulsion droplets (Fig. 1) (29). Localization of ActA protein to the water-oil interface activated Arp2/3-mediated nucleation of branched actin filaments (Fig. 1B), generating homogeneous, ~1-μm-thick cortical actin networks. These networks exhibit continuous actin turnover with a typical time scale of ~1 min (fig. S1), confirming earlier results (29), as well as myosin-driven network dynamics in a stable cell-like geometry. Droplets were flattened and confined between hydrophobic coverslips for observation, thus allowing us to observe the dynamics in a simple 2D geometry, avoiding the complex 3D geometry of the cell membrane. The droplets were ~100 μm in diameter and had a fixed height of 30 μm. The cortical

Fig. 1. Dynamic model actin cortices. Quasi-2D actin networks were generated by encapsulating *Xenopus* egg extract in water-in-oil emulsion droplets and confining actin polymerization to the interface. (**A**) Equatorial cross section of flattened droplets. Simultaneous confocal imaging of Bodipy-conjugated ActA (green, left) and rhodamine-labeled actin (magenta, right). Amphiphilic Bodipy-ActA localizes to the water-oil interface and catalyzes the formation of a quasi-2D dynamic actin network by local activation of Arp2/3. (**B**) Top: Schematic of the experiment. Cortical dynamics are tracked near the flat bottom surface of the droplet. There is continuous turnover between the thin polymeric actin layer and actin monomers in the bulk (arrows). Bottom: Zoomed-in schematic of the essential components of the cortex. IR fluorescent SWNTs are inserted as probes of cortex dynamics.

actin networks were imaged by confocal microscopy (Fig. 1A). To resolve network dynamics with high spatiotemporal resolution, we used near-infrared (IR) fluorescent SWNTs as probes (Fig. 1B). SWNTs are ~1 nm in diameter and ~100 to 300 nm in length (*21*). We found that SWNTs easily penetrate the thin cortex without perturbing the network and, due to their large aspect ratio (*30*), get entrapped long enough to report on network dynamics. Because of their extreme photostability, the SWNTs could be tracked over a broad range of time scales (milliseconds to hours).

In droplets of unmodified diluted extract, we observed homogeneous cortices (Fig. 1A) with no discernible network movement. It is expected that myosins can only drive large-scale movement when the network is sufficiently cross-linked. Therefore, we increased network connectivity by adding an actin cross-linker, α-actinin. We found that, as a function of cross-linker concentration, we could drive the system into three markedly different dynamic steady states, referred to as low, intermediate, and high connectivity (Fig. 2).

At low connectivity (0 to 1.5 μM of added α-actinin), cortices remained homogeneous, and SWNTs fluctuated randomly (Fig. 2A

and movie S1). The homogenous actin distribution reflects a dynamic steady state, with continuous actin polymerization catalyzed by ActA at the surface, balanced by continuous depolymerization to the bulk (fig. S1). Control experiments with myosin-immunodepleted extracts showed that the spatially uncorrelated and random probe motions were largely motor-driven rather than thermally driven (fig. S2).

At intermediate connectivity (2.0 to 2.5 μM of added α-actinin), coherently moving clusters of SWNTs appeared with diameters of up to 10 μm and typical speeds of ~10 μm/min. We did not observe any major changes of cluster sizes during our observation times. Strikingly, the clusters moved over long distances within the cortex without generating large-scale density inhomogeneities in the actin distribution (Fig. 2B and movie S2). Consistently, the SWNT probes moved in a divergence-free manner. That is, on the scale of the whole droplet, the flow was purely vortical (fig. S3). This motion was likely driven by myosin-generated contractile forces acting between clusters. We observed occasional rapid changes of cluster velocities (movie S3) that can be explained by the rupture of tenuous actin bridges between clusters, contracted by few myosin minifilaments. These rupture events in conjunction with actin turnover are likely to be the mechanism for limiting cluster size and maintaining homogeneity.

At high connectivity (3.0 to 4.0 μM of added α-actinin), cortices phase-separated and formed a large cap, which extended over a substantial fraction of the droplet surface but remained essentially 2D. Small clusters continuously nucleated and were then pulled radially toward the cap. This global contraction was visible in both the actin and the SWNT fluorescence channels (Fig. 2C and movies S4 and S5). The velocity of the converging clusters was ~10 μm/min in the periphery and decreased toward the cap (fig. S4 and movie S5). The caps formed at random positions but, once formed, remained stable over several hours. The ratio of intensities between the cap region and peripheral accretion zones also remained constant over time (fig. S5). This shows that the system is still at steady state, maintained by the continuous disassembly of actin from the cap and reassembly in the periphery (movie S5).

An important feature of nonequilibrium dynamic steady states is that they can exhibit order and patterns in structure as well as in motion. We show here that this can lead to intriguing interdependencies where transitions in structure drive transitions in patterns of motion and vice versa. The patterns of motion can be described by a velocity field, which we mapped using the embedded SWNT probes. Order and symmetry breaking in the velocity field reflect the spatial organization of the stress generators. This feature is a distinctly nonequilibrium phenomenon and cannot occur in thermodynamic equilibrium. To quantify this dynamic order, we performed a 2D correlation analysis of SWNT velocities. The analysis shows a rapid but continuous growth of correlation length at intermediate connectivity (fig. S6). Increasing correlation length reflects increasing connectivity in the actin cortex. The shape of the curve (fig. S6) indicates cooperativity. Previously, it has been shown that cross-linking, in combination with contractile motors, can cause an actin network without turnover to break up into individual clusters (*31, 32*). In contrast to those systems, the clusters maintain their size in our nonequilibrium steady-state system but are dynamic, with their lifetime exceeding that of their components.

At intermediate connectivity, patterns of motions fluctuate strongly (movie S2 and Fig. 2B). To quantify fluctuations, we computed changes of velocity in fixed positions in the cortex. We calculated the normalized coarse-grained velocity fluctuation autocorrelation in
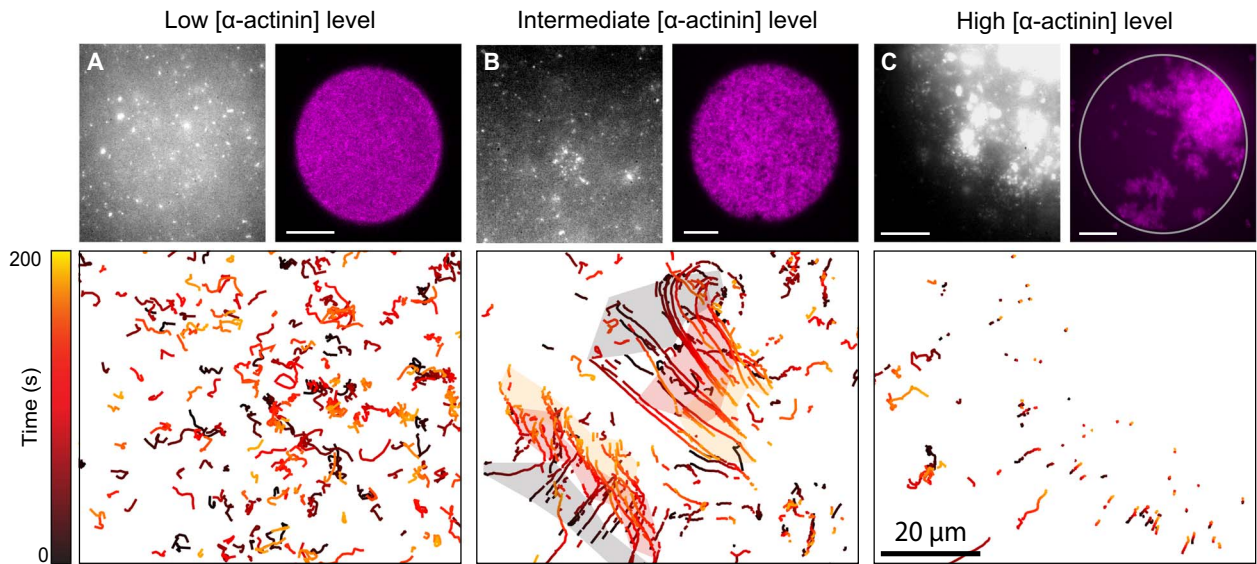
Fig. 2. Signatures of distinct steady states. Network percolation can be induced by increasing cross-linker density (α-actinin). Three distinct steady states can be identified on the basis of qualitative differences in collective network dynamics imaged in the bottom cortical layer in the droplets. (**A**) Low cross-linking (0 to 1.5 μM of added α-actinin; images shown, 1.5 μM). (**B**) Intermediate cross-linking (2 to 2.5 μM of added α-actinin; images shown, 2.5 μM). The colored patches delineate the particles that moved as clusters at time points gray (10 s), red (100 s), and yellow (200 s; movie S2). (**C**) High cross-linking (3 to 4 μM of added α-actinin; images shown, 3 μM). (A to C) Top left: Fluorescence image of inserted SWNT probes. Top right: Confocal image of the actin distribution. Bottom: Individual SWNTs were tracked in 200-s-long movies with 2000 frames (movies S1 to S4). Tracks of individual SWNTs color-coded for progression in time. In the high-connectivity state, the fraction of SWNTs that were accumulated in the cap has not been tracked because of the high density. Scale bar, 20 μm.

time (Fig. 3A), $\tilde{C}_\Delta(\tau) = \langle \Delta \hat{V}_\alpha(t) \cdot \Delta \hat{V}_\alpha(t + \tau) \rangle_{\alpha T}$. The velocity fluctuation, $\Delta \vec{V}$, is the difference between the average velocity in a given coarse-grained box at time t, $\vec{V}_\alpha(t)$, and the time-averaged velocity in the same box $\langle \vec{V}_\alpha \rangle_T$ (see Materials and Methods). Figure 3A shows the velocity fluctuation autocorrelation in time at the different cross-linker concentrations. Local time-averaged velocities are close to zero at low and intermediate connectivity but are nonzero and converging to the cap at high connectivity. Fluctuations have small amplitudes and are rapid at low connectivity, but gain amplitude and persistence at intermediate connectivity, to become of small amplitude again at high connectivity. We constructed a dynamic order parameter to quantify the persistence of local velocities. This scalar order parameter was calculated as the angular correlation of velocities in the coarse-grained boxes, $\langle \cos\phi \rangle_{50s}$, averaged over time intervals of 50 s, longer than the correlation time of the force generated by a myosin minifilament [~5 s (21); Fig. 3B]. The order parameter shows a steep increase at intermediate connectivity. This increasing collective order in probe particle velocities reflects spatial ordering of the local stresses. The cortex, in principle, is viscoelastic, that is, the response will depend on time scales. However, the rapid turnover of the components makes the network behave like a fluid at the time scales of the observed motions. This allows us to directly infer the underlying (slowly varying) part of the stress field from the velocity field. To characterize the observed structural symmetry breaking, we further constructed an actin density–based order parameter. We determined the relative numbers of homogeneous and symmetry-broken cortices at a given cross-linker concentration, inferred from images of rhodamine-labeled actin (Fig. 3C and fig. S7). This order parameter reflects the global structural transition at high connectivity. Three points are important to emphasize: First, the experiments show that dynamic symmetry breaking occurs before structural symmetry breaking (Fig. 3B and fig. 3C). Second, the observed dynamic order is not caused by an underlying nematic ordering

of the actin filaments in the network. Networks of short actin filaments generated by Arp2/3 nucleation are known to be branched and highly disordered (33). Therefore, the dynamics in our model cortices are different from the observed phenomena in highly concentrated motor-activated solutions of actin filaments (34) or microtubules (35), where order is imposed through steric repulsion between long filaments. Third, the mechanism of force generation in our experiments is also different from that of active swimmers (36), such as fish in a school, where particles propel themselves by exerting a force against an embedding medium or a surface.

A remarkable consequence of the interdependence between structural and stress patterns is the emergence of mesoscopic length scales in the system. To extract the average spatial extent of correlated velocity fluctuations driven by the fluctuating arrangements of stress-generating motors, we used the deviations from the average local velocity. The normalized velocity fluctuation correlation function in space (see Materials and Methods; Fig. 3D) was calculated as $\tilde{C}_\Delta(R) = \langle \Delta \hat{v}_i(\vec{r}_i, t) \cdot \Delta \hat{v}_j(\vec{r}_j, t) \delta(|\vec{r}_i - \vec{r}_j| - R) \rangle_{ijT}$. Velocity fluctuation, $\Delta \vec{v}_i$, is the difference between the velocity of an individual particle $\vec{v}_i$ and the average velocity in the coarse-grained box α containing particle i, $\langle \vec{V}_\alpha \rangle_T$ (see Materials and Methods). At low connectivity, spatial correlations of velocity fluctuations are small. At high connectivity, deviations from the local average velocity, which is zero in the cap region and nonzero in the periphery, are also small so that correlations get buried in the noise. At intermediate cross-link densities, however, $\tilde{C}_\Delta(R)$ shows a characteristic fluctuation correlation length of ~15 μm, more than an order of magnitude larger than molecular length scales and smaller than but approaching the system size (Fig. 3E).

The observed velocity fluctuations represent the response of the system to the force fluctuations arising from the myosin activity. Hence, this response provides a measure of the susceptibility of the system to the internally generated active stresses. It has been theoretically
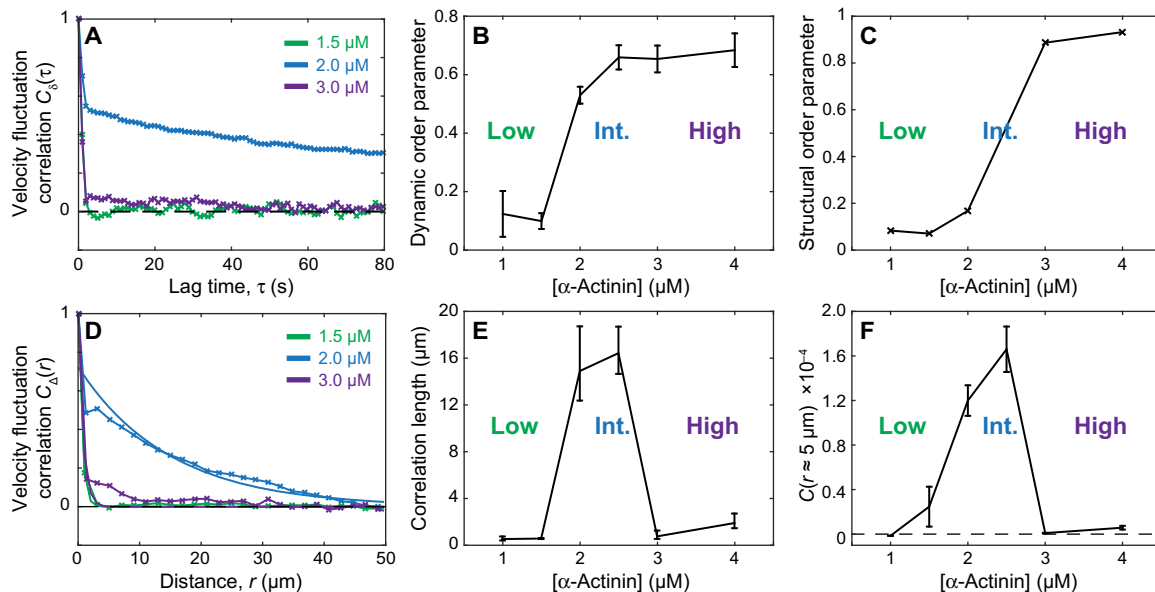
Fig. 3. Collective dynamics and fluctuations. Steady states differ in the degree of order and correlation of probe particle velocities. (**A**) Normalized velocity fluctuation autocorrelation is plotted as a function of lag time for different α-actinin concentrations evaluated in a 5 × 5 coarse-grained grid for 200-s movies, averaged over all grid points. (**B**) Dynamic order parameter calculated from the averaged velocity directional persistence as a function of α-actinin concentration. (**C**) An actin density–based structural order parameter showing the fraction of phase-separated cortices as a function of cross-linker concentration (0 to 4 μM of added α-actinin), inferred from images of actin fluorescence. (**D**) The normalized velocity-velocity fluctuation cross-correlation at zero lag time is plotted as a function of probe distances for different α-actinin concentrations (symbols). Data are fitted with single exponentials (lines). (**E**) Characteristic correlation lengths from fits in (D) as a function of α-actinin concentrations. Error bars represent 95% confidence interval. (**F**) Susceptibility of cluster motion to stress fluctuations quantified from the amplitude of the velocity-velocity fluctuation correlation taken at $R = 5$ μm, plotted as a function of α-actinin concentration. Error bars correspond to SDs.

predicted for elastic networks (without turnover) that strain fluctuations become long-ranged, that is, that mesoscopic length scales emerge near a point of marginal stability of the network (*37*). Increasing cross-linker concentration drives our experimental system toward connectivity percolation. Note that, in these nonequilibrium steady states, connectivity percolation becomes a time scale–dependent concept. The on/off rate of cross-linkers is the relevant time scale for competing dynamic processes such as network turnover and myosin activity. The intermediate steady state has signatures of marginal connectivity. To characterize the response of the system, we quantify the fluctuations in the observed dynamic order. We calculated the nonnormalized correlation function, $C_\Delta(R)$, of velocity fluctuations $\Delta\vec{v}_i$ at a fixed separation $R \sim 5$ μm, larger than the typical length of a single actin filament (<1 μm). Figure 3F shows that this correlation exhibits a peak at intermediate connectivity. The observed peak in susceptibility is consistent with recent theoretical predictions of critical strain fluctuations driven by active stresses in random networks (*37*). To pursue this comparison, we performed numerical simulations of isotropic Mikado networks in 2D, consisting of randomly placed fibers that resist stretching. Contractile stresses were introduced homogeneously and isotropically (see Materials and Methods). We observed a peak in the correlated strain fluctuations (that is, nonuniform network motion) at intermediate length scales between the network mesh size and the full system size (see fig. S8). The simulation results show how random networks subject to contractile stress exhibit critical-like strain fluctuations and can account for a key feature of our experimentally observed velocity fluctuations. Note that the stress/force fluctuations in this model are not constant. These force fluctuations depend on the network structure, because the motor activity acts on the network as substrate. There is thus a coupling between the local network ri-

gidity and motor stress. In the context of biological function, high susceptibility implies high sensitivity to the regulatory parameters. Thus, these marginal states are likely to be relevant for biological function. Hydrodynamics-based models have predicted ordered patterns in actomyosin gels (*36*, *38*); however, these models lack filament turnover and long-range connectivity. A recent model that includes these essential features might be applicable to our system (*39*).

To characterize the global order and symmetry of stress patterns in the three observed states, we calculated directional velocity correlation functions for the entire sets of data (Fig. 4). This function was constructed by calculating the velocity-velocity directional correlation for each moving probe, with all the surrounding probes, as a function of distance and angle with respect to its own direction of motion, and then averaging over all moving particles in all movies (see Materials and Methods) (*40*).

At low connectivity, stress patterns are fully symmetric, and no correlation is observed (Fig. 4A and fig. S7). At intermediate connectivity, the vector field of probe velocities begins to show curl but no divergence (Fig. 4B and figs. S3 and S9). The inner region of positive correlation in Fig. 4B reports an average cluster size, consistent with cluster size estimated from mapping the area covered by co-moving particles (fig. S10). The breaking of rotational symmetry is evident from the extended positive correlations around 0° and 180°, that is, a finite probability that particles trailing and leading a given particle move in the same direction. Motions in our system are generated by myosin motors; hence, correlated motion implies correlated motors. A myosin minifilament acts as a force dipole. A single dipole breaks rotational symmetry locally. When the orientations of dipoles become correlated, rotational symmetry breaking can extend over larger length scales. This correlated rotational symmetry breaking is characteristic of nematic order. In our
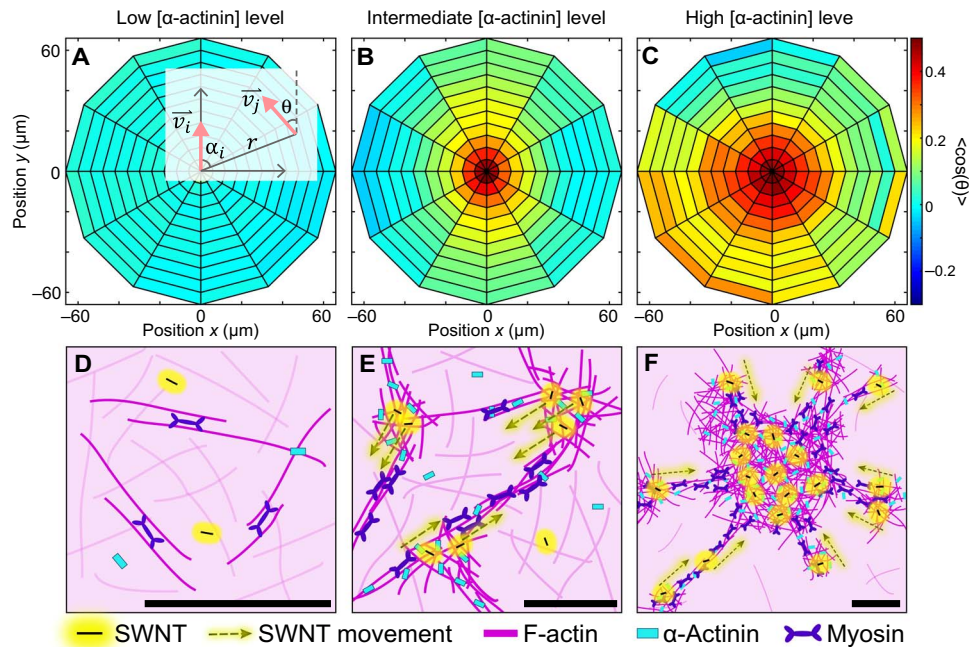
Fig. 4. Order and symmetries in the stress patterns. Increasing cross-linker density leads to increasing order and breaking of symmetries in the arrangement of stress generators. (**A** to **C**) Directional velocity-velocity correlation maps the degree of order and shows breaking of symmetry for increasing α-actinin concentrations. For each concentration, the colors portray the average alignment of pairs of probe velocities, as a function of the distance and angle between them [(A), inset]. At low cross-linking [1 μM; (A)], there is no appreciable correlation. At intermediate connectivity [2.5 μM; (B)], the map shows enhanced correlations, distributed anisotropically, primarily along the front-back axis, signifying the emergence of nematic polar order and the breaking of rotational symmetry. At high connectivity [3 μM; (C)], the converging network flow leads to an asymmetry between top and bottom, indicating the appearance of centrosymmetric polar order and the breaking of translational symmetry. (**D** to **F**) Schematic illustration of the conceptual model for cortex dynamics as a function of connectivity. At low connectivity (D), the network is not mechanically connected, so myosin cannot generate long-range forces, and the network fluctuates randomly. At intermediate connectivity (E), the network reaches the mechanical percolation threshold. Myosin-generated stresses can propagate over larger distances, leading to the formation of rigid clusters, which move in a divergence-free manner. The interplay between stresses and network rearrangement lead to local nematic ordering of the force-generating myosin minifilaments. At high connectivity (F), the network self-organizes into a single large cap with persistent converging flow of clusters into the cap and polar ordering of the myosin force dipoles.

system, nematic order pertains to the stress generators, that is, the myosin force dipoles. As has been pointed out recently in a theory of chromatin hydrodynamics (41), such a stress nematic is not necessarily coupled to a structural nematic. Stresses can self-organize via the network even if the network is disordered. At high connectivity, the velocity vector field around the cap shows divergence rather than curl, which reflects broken translational symmetry due to the formation of the cap (Fig. 4C and fig. S9). The directional correlation function shows, first, an extended correlation length or cap size and, second, an asymmetry between 0° and 180°, which is a signature of a converging flow field (figs. S4 and S11). This converging velocity field likely reflects a radial stress pattern, that is, a radial orientation of myosin force dipoles. This global centrosymmetric polar order is not observed in typical liquid crystals. The crucial difference in our system is the lack of conservation of particles because of continuous actin disassembly in the cap and recycling of monomers to the bulk.

Figure 4 (D to F) presents a conceptual model for the observed nonequilibrium steady states. The generation of order and the breaking of symmetry in the cortex are driven by the interplay of network structure and connectivity and active stresses. Increasing connectivity shifts the time scales of network organization. The longer the network connectivity persists, the more long-range the myosin-generated forces will act. This leads to long-range transport in the cortex and structural rearrangements, which, in turn, feeds back on the arrangement of the force generators themselves. At low connectivity (Fig. 4D), myosin will en-

gage actin but will not drive correlated motions over distances longer than the filament length. At intermediate connectivity (Fig. 4E), the effective range of stress propagation expands. The combination of contractility and cross-linking creates relatively rigid islands of limited size, where the density is not different enough to be visible by actin fluorescence, but the mobility of probe particles within clusters is strongly suppressed. Myosin-activated contractile bridges move the clusters in random and changing directions. Note that competing motors can also accelerate bridge rupture, creating a negative feedback mechanism for cluster growth (movie S3). We speculate that, in our system, in the presence of constant turnover, cluster size (r_c) is primarily limited by the competition between accretion at the boundary ($\propto r_c$) and depolymerization within the cluster ($\propto r_c^2$). At high connectivity (Fig. 4F), a transition occurs when the largest cluster reaches the system size and concentrates actin filaments, motors, and cross-linkers such that a radial gradient emerges. This creates net polymerization in the periphery and net depolymerization in the cap, sets up a steady flow of small clusters towards the cap, and, in turn, orients the motor dipoles radially in the periphery. This model predicts a system size dependence of the second transition.

DISCUSSION
The observed dynamics highlight some of the unique aspects of self-organization of active matter: Internally generated stresses and mechanical structures can couple in complex and subtle ways such

that markedly different dynamic steady states with different structural order can emerge from shifts in the balance between competing time scales. The defining feature of a dynamic steady state is that some parameters remain stationary in the presence of a constant flux of energy, material, or information. This implies that the time scales of the exchange of material, energy, etc. are separated from the duration of the existence of the state. Experiments in living cells have shown that actomyosin cluster formation can be driven by α-actinin cross-linkers, similar to what we find in our model system (42). Dynamic transitions such as cortical symmetry breaking in *Caenorhabditis elegans* (7, 8, 43), the transition into a contractile ring in oocytes (44), membrane stirring (45), or the formation of immunological synapses (46) bear resemblance to our observations. Both the connectivity of the network and the activity of myosin motors can be actively tuned by cells in response to various signals such as Ca^{2+} ions (18, 47). In cells, there is evidence for a broad distribution of actin filament lengths (48). The degree of transient stabilization of filaments (in which it will change the distribution of lengths) is another control parameter with which the cell can shift between the dynamic steady states. The intermediate case of marginal connectivity in our system shows maximal susceptibility to internal stress variations. Because this dynamic symmetry breaking precedes the structural symmetry breaking, it is tempting to speculate on the universality of this principle: The heightened sensitivity associated with these dynamics might facilitate an ensuing major structural reorganization.

MATERIALS AND METHODS
Proteins and reagents
ActA-His-Cys was purified from the strain DP-L4363 of *Listeria monocytogenes* (from J. Theriot, Stanford University) and conjugated with about six to eight molecules of Bodipy FL-X-SE (#D6102, Molecular Probes) per protein, as previously reported (29). ActA-Bodipy was stored at a concentration of ~30 µM at −80°C. Before use, ActA-Bodipy was sonicated on ice for 15 min and centrifuged at 4°C for 15 min at 16,000g to remove aggregates.

Actin was purified from chicken skeletal muscle and labeled in filamentous form with tetramethylrhodamine iodoacetamide (#T6006, Molecular Probes) at a labeling ratio of ~10% using standard protocols. The purified actin was stored at −80°C at a concentration of ~5 mg/ml (~120 µM) in G-buffer [10 mM tris-HCl (pH 8.6), 0.1 mM dithiothreitol, 0.2 mM adenosine 5′-triphosphate (ATP), 0.1 mM $CaCl_2$].

The cross-linker α-actinin was purchased from Cytoskeleton Inc. and reconstituted to a final concentration of 40 µM with water. Crude M-phase extracts and myosin II–immunodepleted extracts were prepared from freshly laid *Xenopus laevis* eggs, as previously described (29).

Single-walled carbon nanotubes
SWNTs were obtained from Rice University's Richard E. Smalley Institute for Nanoscale Science and Technology, which is no longer producing SWNTs. Exactly equivalent material can now be purchased from Sigma-Aldrich [carbon nanotube, single-walled (6,5) chirality, ≥95% carbon basis (≥99% as carbon nanotubes), 0.78-nm average diameter, product number 773735].

One milligram of HiPco SWNTs (batch number 189.2, Rice University) and 2 mg of d(T)30 oligonucleotides (Invitrogen) were added to 2 ml of deionized water in a glass scintillation vial. The vial was placed on ice and sonicated (Vibra-Cell, VC-50; Sonics & Materials) at a power of 10 W at 20 kHz for 90 min using a 2-mm-diameter microprobe tip.

After sonication, the sample was centrifuged at 16,000g for 90 min. The supernatant was carefully collected and filtered using a 4-ml Millipore Amicon ultracentrifuge filter device (molecular weight cutoff, 100 kDa). The SWNT-ssDNA (single-stranded DNA) stock solution was stored at 4°C.

Emulsion preparation
A motility mix was prepared by mixing the following: for a total volume of 10 µl, 4 µl of crude *X. laevis* egg extract, 2 µl of 2×XB buffer [20 mM Hepes (pH 7.7), 10 mM EGTA, 200 mM KCl, 60 mM $MgCl_2$, 0.2 mM $CaCl_2$], 1 µl of SWNT-ssDNA, 1 µl of α-actinin at the appropriate concentration, 1 µl of labeled actin in G-buffer (5 mg/ml), 0.5 µl of ATP regeneration mix (150 mM creatine phosphate, 20 mM ATP, 20 mM $MgCl_2$, and 20 mM EGTA), and 0.5 µl of ActA-Bodipy (30 µM). We estimate the total actin concentration in the motility mix to be ~25 µM. Emulsions were made by adding 1% (v/v) motility mix to mineral oil (Sigma) containing 4% cetyl PEG/PPG-10/1 dimethicone (ABIL EM 90, Evonik Industries), stirring for 1 min on ice, and incubating for an additional 10 min to allow the emulsions to settle. The oil and surfactant mixture was degassed under vacuum overnight before use to reduce phototoxicity. Glass coverslips were passivated by treatment with 10% dichlorodimethylsilane (Fluka) in heptane for 30 min. Samples were made by sandwiching ~15 µl of the emulsion mixture in chambers assembled from two passivated coverslips, separated by a 30-µm double-stick tape (3M), and sealed with VALAP (1:1:1 vaseline/lanolin/paraffin).

In both sets of experiments, the density measurements of fluorescent actin and the network dynamics measurements using SWNTs were done with the same samples. One emulsion was made and split into identical samples that were simultaneously imaged on two different microscopes to follow actin density fluctuations and the SWNT dynamics tracking network fluxes.

Imaging
SWNT imaging setup
(6,5) nanotubes in the sample (excitation, 567 nm/emission, 975 nm) were excited by a high-power 561-nm diode-pumped solid-state laser (DPSS) (500-mW continuous wave; Cobolt Jive, Cobolt) or a tunable Ti:sapphire laser (Mira 900-F, Coherent Inc.). A neutral-density filter (NDC-50C-4M, Thorlabs) served to adjust the intensity of the beam. The beam diameter was expanded using two lenses with focal lengths $f_1 = 40$ mm and $f_2 = 150$ mm (Thorlabs). The beam was circularly polarized using a quarter-wave plate (AQWP05M-600, Thorlabs) and then focused into the back aperture of a high-NA (numerical aperture) objective (alpha Plan-Apochromat, 100×, NA = 1.46; Zeiss). Fluorescence light was collected through the same objective and passed through a dichroic beam splitter (630 DCXXR, AHF analysentechnik), filtered using a 900-nm long-pass filter (F47-900, AHF analysentechnik) and focused onto a short-wave IR camera with an InGaAs detector (XEVA-SHS-1.7-320 TE-1, Xenics). Images of SWNT dynamics were recorded at 10 frames per second, near the bottom coverslip.

Confocal imaging setup
Confocal images of the actin and ActA distribution were acquired on a laser scanning confocal microscope (Leica TCS SP5X) with resonant scanner, avalanche photodiode detectors, galvo-stage, white-light laser, or a 3I spinning disc confocal microscope (Zeiss) running SlideBook software. Images were acquired using a 63× oil objective (NA = 1.4) with laser illumination and appropriate emission filters. Images on the spinning disc confocal microscope were collected with an electron-multiplying charge-coupled device camera (QuantEM, Photometrics).

Data analysis

Using single-particle tracking software u-track (49), we obtained SWNT positions. Only tracks with 70 data points or longer were included in the analysis. Velocities, $\vec{v}_i(\vec{r}_i, t)$, were calculated by linearly interpolating individual particle tracks over 10 frames (1 s) and assigning those velocities to the middle t of the respective time interval. Total recording lengths were 2000 frames, corresponding to a total recording time of $T = 200$ s. For spatial coarse graining, the entire field of view (256 by 312 pixels, 300 nm per pixel) was segmented into a 5×5 grid of boxes. The average velocity at time t in each box, α, was calculated as $\vec{V}_\alpha(t) = \frac{1}{N_\alpha}\sum_{i\in\alpha}\vec{v}_i(\vec{r}_i, t)$, where N_α is the total number of probe particles that fulfilled the selection criterion in the box. The overall average velocity in the coarse-grained box α, $\langle \vec{V}_\alpha \rangle_T$, was calculated by averaging over the whole recording time T.

Calculation of spatial velocity correlations

We first calculated the spatial velocity cross-correlation function at equal times: $C(R) = \langle \vec{v}_i(\vec{r}_i, t) \cdot \vec{v}_j(\vec{r}_j, t)\delta(|\vec{r}_i - \vec{r}_j| - R)\rangle_{ijT}$. Here, $\langle \ldots \rangle_{ijT}$ represents averaging over all possible (i, j) pairs of particles in space and over the whole recording time to obtain a measure for the range of correlated probe particle motion in the cortex.

Faster-moving particles that are not strongly correlated with others can obscure the correlations between more slowly-moving particles because of the large amplitude noise they add to the correlation function. Therefore, we used normalized velocities $\hat{v}_i(\vec{r}_i, t) = \frac{\vec{v}_i(\vec{r}_i, t)}{\|\vec{v}_i(\vec{r}_i, t)\|}$ and then calculated the normalized spatial velocity correlation function as $\tilde{C}(R) = \langle \hat{v}_i(\vec{r}_i, t) \cdot \hat{v}_j(\vec{r}_j, t)\delta(|\vec{r}_i - \vec{r}_j| - R)\rangle_{ijT}$.

To obtain a measure of the variation of velocity in the cortices over the recording intervals, we calculated the velocity fluctuation of an individual particle at position $\vec{r}_i$ and time t, $\Delta\vec{v}_i(\vec{r}_i, t)$ as the difference between the velocity of the individual particle $\vec{v}_i(\vec{r}_i, t)$, and the overall average velocity in the coarse-grained box, α, containing particle i: $\Delta\vec{v}_i(\vec{r}_i, t) = \vec{v}_i(\vec{r}_i, t) - \langle \vec{V}_\alpha \rangle_T$. To quantify the spatial extent of correlated fluctuations away from the average velocity in a given location of the cortex, independent of the magnitude of the fluctuations, it is again useful to define a normalized velocity fluctuation $\Delta\hat{v}_i(\vec{r}_i, t) = \frac{\Delta\vec{v}_i(\vec{r}_i, t)}{\|\Delta\vec{v}_i(\vec{r}_i, t)\|}$. The normalized spatial velocity fluctuation cross-correlation function is then defined as $\tilde{C}_\Delta(R) = \langle \Delta\hat{v}_i(\vec{r}_i, t) \cdot \Delta\hat{v}_j(\vec{r}_j, t)\delta(|\vec{r}_i - \vec{r}_j| - R)\rangle_{ijT}$.

Mechanical susceptibility of cortical actin to internally generated forces by myosin can be estimated from the overall averaged variations of velocity of collective motion. At low cross-linker concentration, velocities varied strongly but were not spatially correlated. Because we are interested in the variations of the correlated velocities, we calculated spatial velocity fluctuation correlations at a fixed distance $R = 5$ μm. This is a distance larger than the typical length of a single actin filament, over which velocities are expected to be correlated even at low cross-linker concentration. To estimate susceptibility, we used the non-normalized cross-correlation to detect amplitude variations $C_\Delta(R = 5$ μm$) = \langle \vec{v}_i(\vec{r}_i, t) \cdot \vec{v}_j(\vec{r}_j, t)\delta(|\vec{r}_i - \vec{r}_j| - 5$ μm$)\rangle_{ijT}$.

Calculation of temporal velocity autocorrelation

Using normalized averaged velocity fluctuations in the coarse-grained boxes $\Delta\hat{V}_\alpha(t) = \frac{[\vec{V}_\alpha(t) - \langle \vec{V}_\alpha \rangle_T]}{\|\vec{V}_\alpha(t) - \langle \vec{V}_\alpha \rangle_T\|}$, we calculated temporal velocity autocorrelation as $\tilde{C}_\Delta(\tau) = \langle \Delta\hat{V}_\alpha(t) \cdot \Delta\hat{V}_\alpha(t + \tau)\rangle_{\alpha T}$. Here, $\langle \ldots \rangle_{\alpha T}$ represents averaging over all coarse-grained boxes α and over the total recording time T. The scalar dynamic order parameter was defined as $\langle \cos\phi \rangle_{50s} = \langle V_\alpha(t) \cdot V_\alpha(t + 50s) \rangle_{\alpha T}$.

Calculation of directional velocity correlation

To obtain a quantitative and averaged measure for the symmetry of the patterns of motion of the probe particles, we took the point of view of an individual particle and asked how other particles move as a function of their distance and angles with respect to the direction of motion of the reference particle motion. This analysis was performed for every moving probe particle and then averaged over all particles and the total recording time. The directional velocity correlation is defined accordingly as $\tilde{C}_{dir}(R\theta) = \langle \hat{v}_i(\vec{r}_i, t) \cdot \hat{v}_j(\vec{r}_j, t)\delta(\theta - \theta_{ij})\rangle_{ijT}$.

Here, θ_{ij} is defined locally via $\cos\theta_{ij} = \frac{\hat{v}_{ij} \cdot (\vec{r}_i - \vec{r}_j)}{\|\vec{r}_i - \vec{r}_j\|}$. Note that $\theta_{ij} \neq \theta_{ji}$. This procedure corresponds to a transformation of the velocity field into a coordinate system that co-rotates with the local direction of the motion of the respective reference particle. The output is an angularly resolved correlation map that allows extracting the velocity-velocity correlation in any given direction relative to the direction of motion of the reference particle (40).

Calculation of cluster size

To determine the cluster size at intermediate cross-link density, we first manually selected a long particle track belonging to the cluster of interest. All other tracks with constant relative distance to the first track with some tolerance (over the duration in which both tracks are simultaneously present) are considered to belong to the same cluster. Once all particle tracks belonging to the same cluster are identified, the cluster size as a function of time (fig. S10) was determined by finding the convex hull of all identified particles in a particular frame, using the MATLAB function convhull. Clusters were defined by a relatively small number of tracked probe particles. Appearance or disappearance of individual probe particles causes the abrupt steps in cluster size. By visual inspection, all clusters remained largely intact for the duration of experiment and no complete dissolution of clusters was observed.

SUPPLEMENTARY MATERIALS

Supplementary material for this article is available at http://advances.sciencemag.org/cgi/content/full/4/6/eaar2847/DC1

Simulations
fig. S1. Actin turnover.
fig. S2. Control experiments with myosin-immunodepleted extracts.
fig. S3. Curl field of intermediate cross-link regime.
fig. S4. Divergence field of high cross-link regime.
fig. S5. Cortex at steady state.
fig. S6. Velocity correlation.
fig. S7. Symmetry breaking of cortices with addition of cross-linker.
fig. S8. Simulations.
fig. S9. Density current maps.
fig. S10. Cluster size development with time.
fig. S11. Order and symmetries in the stress patterns of the high cross-link concentration.
movie S1. Motion of SWNTs in the cortex at low connectivity (1.5 μM of added α-actinin).
movie S2. Motion of SWNTs in the cortex at intermediate connectivity (2.5 μM of added α-actinin).
movie S3. Motion of SWNTs in the cortex at intermediate connectivity (2.5 μM of added α-actinin).
movie S4. Motion of SWNTs in the cortex at high connectivity (3.0 μM of added α-actinin).
movie S5. Rhodamine-labeled actin cortices at high connectivity (3.0 μM of added α-actinin) phase-separate and form a large cap, which extend over a substantial fraction of the droplet surface.

REFERENCES AND NOTES

1. G. Salbreux, G. Charras, E. Paluch, Actin cortex mechanics and cellular morphogenesis. *Trends Cell Biol.* **22**, 536–545 (2012).
2. K. J. Chalut, E. K. Paluch, The actin cortex: A bridge between cell shape and function. *Dev. Cell* **38**, 571–573 (2016).

3. S. Mukhina, Y. l. Wang, M. Murata-Hori, α-Actinin is required for tightly regulated remodeling of the actin cortical network during cytokinesis. *Dev. Cell* **13**, 554–565 (2007).

4. E. M. Reichl, Y. Ren, M. K. Morphew, M. Delannoy, J. C. Effler, K. D. Girard, S. Divi, P. A. Iglesias, S. C. Kuo, D. N. Robinson, Interactions between myosin and actin crosslinkers control cytokinesis contractility dynamics and mechanics. *Curr. Biol.* **18**, 471–480 (2008).

5. T. D. Pollard, J. A. Cooper, Actin, a central player in cell shape and movement. *Science* **326**, 1208–1212 (2009).

6. M. Fritzsche, A. Lewalle, T. Duke, K. Kruse, G. Charras, Analysis of turnover dynamics of the submembranous actin cortex. *Mol. Biol. Cell* **24**, 757–767 (2013).

7. E. Munro, B. Bowerman, Cellular symmetry breaking during *Caenorhabditis elegans* development. *Cold Spring Harb. Perspect. Biol.* **1**, a003400 (2009).

8. M. Mayer, M. Depken, J. S. Bois, F. Jülicher, S. W. Grill, Anisotropies in cortical tension reveal the physical basis of polarizing cortical flows. *Nature* **467**, 617–621 (2010).

9. Y. H. Tee, T. Shemesh, V. Thiagarajan, R. F. Hariadi, K. L. Anderson, C. Page, N. Volkmann, D. Hanein, S. Sivaramakrishnan, M. M. Kozlov, A. D. Bershadsky, Cellular chirality arising from the self-organization of the actin cytoskeleton. *Nat. Cell Biol.* **17**, 445–457 (2015).

10. R. D. Mullins, Cytoskeletal mechanisms for breaking cellular symmetry. *Cold Spring Harb. Perspect. Biol.* **2**, a003392, (2010).

11. K. Carvalho, J. Lemière, F. Faqir, J. Manzi, L. Blanchoin, J. Plastino, T. Betz, C. Sykes, Actin polymerization or myosin contraction: Two ways to build up cortical tension for symmetry breaking. *Philos. Trans. R. Soc. Lond. B Biol. Sci.* **368**, 20130005 (2013).

12. A. C. Martin, M. Kaschube, E. F. Wieschaus, Pulsed contractions of an actin–myosin network drive apical constriction. *Nature* **457**, 495–499 (2009).

13. D. Mizuno, R. Bacabac, C. Tardin, D. Head, C. F. Schmidt, High-resolution probing of cellular force transmission. *Phys. Rev. Lett.* **102**, 168102 (2009).

14. M. Roh-Johnson, G. Shemer, C. D. Higgins, J. H. McClellan, A. D. Werts, U. S. Tulu, L. Gao, E. Betzig, D. P. Kiehart, B. Goldstein, Triggering a cell shape change by exploiting preexisting actomyosin contractions. *Science* **335**, 1232–1235 (2012).

15. S. R. Naganathan, S. Fürthauer, M. Nishikawa, F. Jülicher, S. W. Grill, Active torque generation by the actomyosin cell cortex drives left-right symmetry breaking. *eLife* **3**, e04165 (2014).

16. A. Saha, M. Nishikawa, M. Behrndt, C.-P. Heisenberg, F. Jülicher, S. W. Grill, Determining physical properties of the cell cortex. *Biophys. J.* **110**, 1421–1429 (2016).

17. G. T. Charras, M. Coughlin, T. J. Mitchison, L. Mahadevan, Life and times of a cellular bleb. *Biophys. J.* **94**, 1836–1853 (2008).

18. M. A. Conti, R. S. Adelstein, Nonmuscle myosin II moves in new directions. *J. Cell Sci.* **121**, 11–18 (2008).

19. D. A. Fletcher, R. D. Mullins, Cell mechanics and the cytoskeleton. *Nature* **463**, 485–492 (2010).

20. H. Ennomani, G. Letort, C. Guérin, J.-L. Martiel, W. Cao, F. Nédélec, E. M. De La Cruz, M. Théry, L. Blanchoin, Architecture and connectivity govern actin network contractility. *Curr. Biol.* **26**, 616–626 (2016).

21. N. Fakhri, A. D. Wessel, C. Willms, M. Pasquali, D. R. Klopfenstein, F. C. MacKintosh, C. F. Schmidt, High-resolution mapping of intracellular fluctuations using carbon nanotubes. *Science* **344**, 1031–1035 (2014).

22. M. Fritzsche, C. Erlenkämper, E. Moeendarbary, G. Charras, K. Kruse, Actin kinetics shapes cortical network structure and mechanics. *Sci. Adv.* **2**, e1501337 (2016).

23. S. Köhler, K. M. Schmoller, A. H. Crevenna, A. R. Bausch, Regulating contractility of the actomyosin cytoskeleton by pH. *Cell Rep.* **2**, 433–439 (2012).

24. M. Murrell, M. L. Gardel, Actomyosin sliding is attenuated in contractile biomimetic cortices. *Mol. Biol. Cell* **25**, 1845–1853 (2014).

25. D. V. Köster, K. Husain, E. Iljazi, A. Bhat, P. Bieling, R. D. Mullins, M. Rao, S. Mayor, Actomyosin dynamics drive local membrane component organization in an in vitro active composite layer. *Proc. Natl. Acad. Sci. U.S.A.* **113**, E1645–E1654 (2016).

26. M. Krieg, Y. Arboleda-Estudillo, P.-H. Puech, J. Käfer, F. Graner, D. J. Müller, C.-P. Heisenberg, Tensile forces govern germ-layer organization in zebrafish. *Nat. Cell Biol.* **10**, 429–436 (2008).

27. J.-Y. Tinevez, U. Schulze, G. Salbreux, J. Roensch, J.-F. Joanny, E. Paluch, Role of cortical tension in bleb growth. *Proc. Natl. Acad. Sci. U.S.A.* **106**, 18581–18586 (2009).

28. D. Mizuno, C. Tardin, C. F. Schmidt, F. C. MacKintosh, Nonequilibrium mechanics of active cytoskeletal networks. *Science* **315**, 370–373 (2007).

29. E. Abu Shah, K. Keren, Symmetry breaking in reconstituted actin cortices. *eLife* **3**, e01433 (2014).

30. N. Fakhri, F. C. MacKintosh, B. Lounis, L. Cognet, M. Pasquali, Brownian motion of stiff filaments in a crowded environment. *Science* **330**, 1804–1807 (2010).

31. S. Köhler, V. Schaller, A. R. Bausch, Structure formation in active networks. *Nat. Mater.* **10**, 462–468 (2011).

32. J. Alvarado, M. Sheinman, A. Sharma, F. C. MacKintosh, G. H. Koenderink, Molecular motors robustly drive active gels to a critically connected state. *Nat. Phys.* **9**, 591–597 (2013).

33. L. Blanchoin, K. J. Amann, H. N. Higgs, J.-B. Marchand, D. A. Kaiser, T. D. Pollard, Direct observation of dendritic actin filament networks nucleated by Arp2/3 complex and WASP/Scar proteins. *Nature* **404**, 1007–1011 (2000).

34. V. Schaller, C. Weber, C. Semmrich, E. Frey, A. R. Bausch, Polar patterns of driven filaments. *Nature* **467**, 73–77 (2010).

35. T. Sanchez, D. T. N. Chen, S. J. DeCamp, M. Heymann, Z. Dogic, Spontaneous motion in hierarchically assembled active matter. *Nature* **491**, 431–434 (2012).

36. M. C. Marchetti, J. F. Joanny, S. Ramaswamy, T. B. Liverpool, J. Prost, M. Rao, R. A. Simha, Hydrodynamics of soft active matter. *Rev. Mod. Phys.* **85**, 1143–1189 (2013).

37. M. Sheinman, C. P. Broedersz, F. C. MacKintosh, Actively stressed marginal networks. *Phys. Rev. Lett.* **109**, 238101 (2012).

38. J. Prost, F. Jülicher, J.-F. Joanny, Active gel physics. *Nat. Phys.* **11**, 111–117 (2015).

39. D. S. Banerjee, A. Munjal, T. Lecuit, M. Rao, Actomyosin pulsation and flows in an active elastomer with turnover and network remodeling. *Nat. Commun.* **8**, 1121 (2017).

40. H. P. Zhang, A. Be'er, E.-L. Florin, H. L. Swinney, Collective motion and density fluctuations in bacterial colonies. *Proc. Natl. Acad. Sci. U.S.A.* **107**, 13626–13630 (2010).

41. R. Bruinsma, A. Y. Grosberg, Y. Rabin, A. Zidovska, Chromatin hydrodynamics. *Biophys. J.* **106**, 1871–1881 (2014).

42. D. Li, L. Shao, B.-C. Chen, X. Zhang, M. Zhang, B. Moses, D. E. Milkie, J. R. Beach, J. A. Hammer III, M. Pasham, T. Kirchhausen, M. A. Baird, M. W. Davidson, P. Xu, E. Betzig, Extended-resolution structured illumination imaging of endocytic and cytoskeletal dynamics. *Science* **349**, aab3500 (2015).

43. M. Nishikawa, S. R. Naganathan, F. Jülicher, S. W. Grill, Controlling contractile instabilities in the actomyosin cortex. *eLife* **6**, e19595 (2017).

44. W. M. Bement, M. Leda, A. M. Moe, A. M. Kita, M. E. Larson, A. E. Golding, C. Pfeuti, K.-C. Su, A. L. Miller, A. B. Goryachev, G. von Dassow, Activator–inhibitor coupling between Rho signalling and actin assembly makes the cell cortex an excitable medium. *Nat. Cell Biol.* **17**, 1471–1483 (2015).

45. R. Raghupathy, A. A. Anilkumar, A. Polley, P. P. Singh, M. Yadav, C. Johnson, S. Suryawanshi, V. Saikam, S. D. Sawant, A. Panda, Z. Guo, R. A. Vishwakarma, M. Rao, S. Mayor, Transbilayer lipid interactions mediate nanoclustering of lipid-anchored proteins. *Cell* **161**, 581–594 (2015).

46. T. Ilani, G. Vasiliver-Shamis, S. Vardhana, A. Bretscher, M. L. Dustin, T cell antigen receptor signaling and immunological synapse stability require myosin IIA. *Nat. Immunol.* **10**, 531–539 (2009).

47. K. Burridge, J. R. Feramisco, Non-muscle α-actinins are calcium-sensitive actin-binding proteins. *Nature* **294**, 565–567 (1981).

48. L. Blanchoin, R. Boujemaa-Paterski, C. Sykes, J. Plastino, Actin dynamics, architecture, and mechanics in cell motility. *Physiol. Rev.* **94**, 235–263 (2014).

49. K. Jaqaman, D. Loerke, M. Mettlen, H. Kuwata, S. Grinstein, S. L Schmid, G. Danuser, Robust single-particle tracking in live-cell time-lapse sequences. *Nat. Methods* **5**, 695–702 (2008).

Science Advances

Self-organized stress patterns drive state transitions in actin cortices

Tzer Han Tan, Maya Malik-Garbi, Enas Abu-Shah, Junang Li, Abhinav Sharma, Fred C. MacKintosh, Kinneret Keren, Christoph F. Schmidt, and Nikta Fakhri

View the article online
https://www.science.org/doi/10.1126/sciadv.aar2847
Permissions
https://www.science.org/help/reprints-and-permissions

Use of this article is subject to the Terms of service